Geophysical Journal International

Geophys. J. Int. (2020) **223,** 1327–1337
Advance Access publication 2020 August 10
GJI Seismology

doi: 10.1093/gji/ggaa364

Compaction of the Groningen gas reservoir investigated with train noise

Wen Zhou and Hanneke Paulssen

Department of Earth Sciences, Utrecht University, Princetonlaan 8A, 3584 CB Utrecht, The Netherlands. E-mail: w.zhou@uu.nl

Accepted 2020 July 28. Received 2020 July 25; in original form 2020 May 14

SUMMARY

Induced seismicity in the Groningen gas field in the Netherlands has been related to reservoir compaction caused by gas pressure depletion. *In situ* measurement of compaction is therefore relevant for seismic hazard assessment. In this study, we investigated the potential of passively recorded deep borehole noise data to detect temporal variations in the Groningen reservoir. Train signals recorded by an array of 10 geophones at reservoir depth were selected from the continuous noise data for two 5-month deployments in 2015. Interferometry by deconvolution was applied to the high-frequency train signals that acted as stable, repetitive noise sources. Direct intergeophone *P* and *S* wave traveltimes were then used to construct the *P*- and *S*-wave velocity structure along the geophone array. The resulting models agree with independently obtained velocity profiles and have very small errors. Most intergeophone *P* wave traveltimes showed decreasing traveltimes per deployment period, suggestive of compaction. However, the retrieved traveltime changes are very small, up to tens of microseconds per deployment period, with uncertainties that are of similar size, about 10 microseconds. An unambiguous interpretation in terms of compaction is therefore not warranted, although the 10 μs error per 5-month period is probably smaller than can be achieved from active time-lapse seismic surveys that are commonly used to measure reservoir compaction. The direct *P*-wave amplitudes of the train-signal deconvolutions were investigated for additional imprints of compaction. Whereas the *P*-wave amplitudes consistently increased during the second deployment, suggestive of compaction, no such trend was observed for the first deployment, rendering the interpretation of compaction inconclusive. Our results therefore present hints, but no obvious effects of compaction in the Groningen reservoir. Yet, this study demonstrates that the approach of deconvolution interferometry applied to deep borehole data allows monitoring of small temporal changes in the subsurface for stable repetitive noise sources such as trains.

Key words: Induced seismicity; Seismic interferometry; Seismic noise.

1 INTRODUCTION

The Groningen gas field in the Netherlands is one of the largest onshore gas fields in the world. Production started in 1963 and the first recorded induced earthquake occurred in 1991 (van Eck *et al.* 2006). Seismicity remained rather low in the following years, with about five earthquakes ($1.5 \leq M_L \leq 2.7$) per year, but increased with increasing production between 2003 and 2013, the year of the largest (M_L=3.6) earthquake to date (Van Thienen-Visser & Breunese 2015). It has been suggested that reservoir compaction due to pore pressure reduction by gas extraction plays a dominant role inducing the seismicity (e.g. Bourne *et al.* 2014; Candela *et al.* 2018). The region of highest seismicity indeed roughly corresponds to the region of largest subsidence (Fig. 1). Monitoring the temporal variations of the reservoir is essential to calibrate mechanical models that relate compaction to the extraction of gas. Experimental studies have shown that the mechanical behaviour of the reservoir rock in response to pressure depletion is more complex than simple elastic shortening (Pijnenburg *et al.* 2018, 2019). It is therefore important to have *in situ* measurements of reservoir compaction. Some measurements have been obtained from downhole radioactive markers (Kole 2015) and, more recently, from distributed strain sensing (DSS, Cannon & Kole 2018). It would be beneficial to investigate if compaction can be determined independently from seismic data.

A large number of studies have shown that it is possible to detect temporal changes in subsurface properties from changes in the seismic wavefield. Seismic velocity changes associated with earthquakes have been measured in various ways: actively in a cross-well experiment (Silver *et al.* 2007; Niu *et al.* 2008) as well as passively using different approaches (e.g. Yamada *et al.* 2010; Nakata & Snieder 2011; Pei *et al.* 2019). Time-lapse 3-D seismic surveys

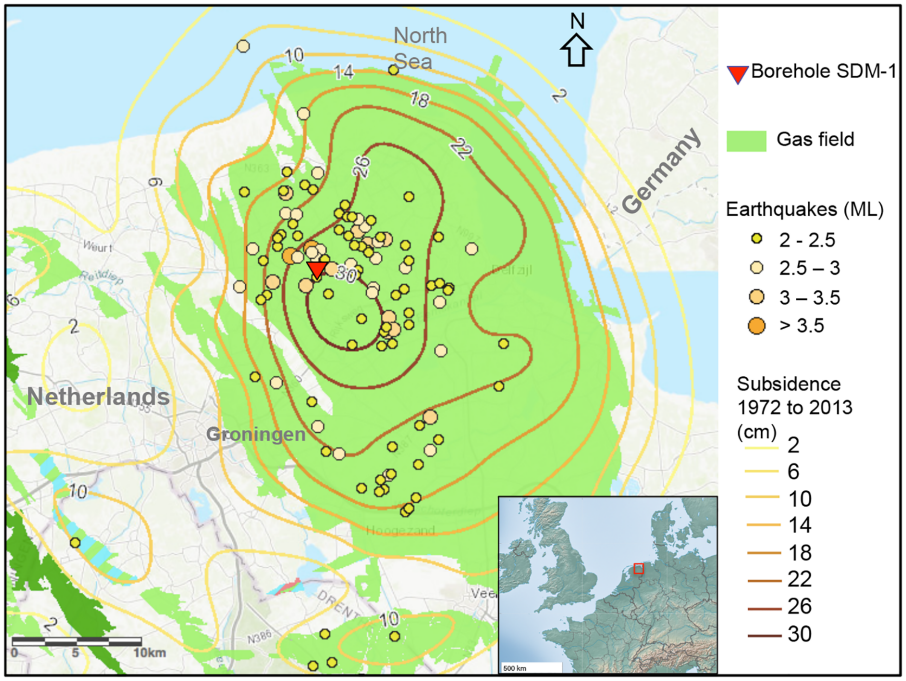

Figure 1. Seismicity and subsidence of the Groningen field (modified from NAM 2020). Earthquakes (1991–2019, $M_L > 2$) are retrieved from the KNMI catalog (KNMI 2020). Surface subsidence is obtained from levelling measurements between 1972 and 2013 (NAM 2018). The location of borehole SDM-1 is marked with a red triangle.

revealed traveltime changes in and around oil or gas reservoirs (e.g. Hatchell & Bourne 2005; MacBeth *et al.* 2018) and reservoirs for CO_2 storage (e.g. Boait *et al.* 2012). Minor changes in the medium can be inferred from the coda of ambient noise auto- or cross-correlations, and studies of coda-wave interferometry have revealed seismic velocity changes caused by the solid-earth tides (Sens-Schönfelder & Eulenfeld 2019) and earthquakes (e.g. Wegler & Sens-Schönfelder 2007; Brenguier *et al.* 2008), in buildings (e.g. Nakata *et al.* 2013) or other structures (e.g. Salvermoser *et al.* 2015). However, coda-wave interferometry has limitations localizing the sources of the detected changes in the medium, although approaches have been suggested to solve this problem (Larose *et al.* 2010; Obermann *et al.* 2019). Compared to coda-wave studies, interferometric studies that use direct (ballistic) waves to identify temporal variations provide a better spatial resolution. Recently, Brenguier *et al.* (2020) and Mordret *et al.* (2020) inferred temporal velocity variations in the shallow Groningen subsurface from ballistic body and surface waves obtained from ambient noise data of a dense surface geophone network. Variations in the 3-km-deep subsurface can not be obtained from surface sensors, but Behm (2017) suggested that it should be possible using noise recordings from deep downhole arrays.

In 2013, two monitoring wells in the Groningen gas field were equipped with geophone arrays in the reservoir at 3 km depth. Zhou & Paulssen (2017) determined the *P*- and *S*-wave velocity structure along the geophone array of one of these boreholes with noise interferometry by cross-correlation. They further found that diurnal variations in anthropogenic noise had a strong impact on the interferograms, impeding the detection of temporal velocity variations in the reservoir. However, they suggested that high-frequency repetitive noise signals generated by passing trains might allow more stable and higher accuracy traveltime measurements. Trains are well-known sources of strong vibrations (Chen *et al.* 2004; Fuchs & Bokelmann 2018), and seismic interferometry has previously been applied to train signals (Quiros *et al.* 2016; Zhang *et al.* 2019). Moreover, Brenguier *et al.* (2019) showed the potential of train-signal interferometry for monitoring temporal velocity changes associated with active faults. To our knowledge, the study presented here is the first that employs train noise recorded by a deep borehole geophone array.

2 BOREHOLE DATA AND TRAIN SIGNALS

The data that are used in this study are from a deep borehole geophone array at reservoir level at 3 km depth. The operator of the gas field, the Nederlandse Aardolie Maatschappij (NAM), deployed a string of 10 geophones in well SDM-1 during two 5-month periods in 2015 (January 23–June 29 and July 3–December 1). The well is located in the Loppersum area of the Groningen gas field, a region that experienced a high level of seismicity and subsidence (Fig. 1). Three-component 15-Hz geophones were positioned at depths from 2750 to 3000 m (Fig. 2a), with 30 m intergeophone spacings from the top geophone (GP01) to geophone 9 (GP09) and 15 m between GP09 and lowest geophone (GP10). The geophones are positioned at the same depths for the two deployments and there is only a small time gap of 4 d between the two deployment periods. The setting is presented in Fig. 2(b) showing the location of the borehole at ∼500 m distance from the railway track which links the towns Stedum and Loppersum. Note that the vertical distance between railway track and geophone array is six times larger than the horizontal distance, implying close-to-vertical propagation of train noise along the geophone array.

Two examples of train noise recordings are presented in Fig. 3. The figure shows the vertical component seismograms (filtered between 30 and 120 Hz) for a train from Stedum to Loppersum

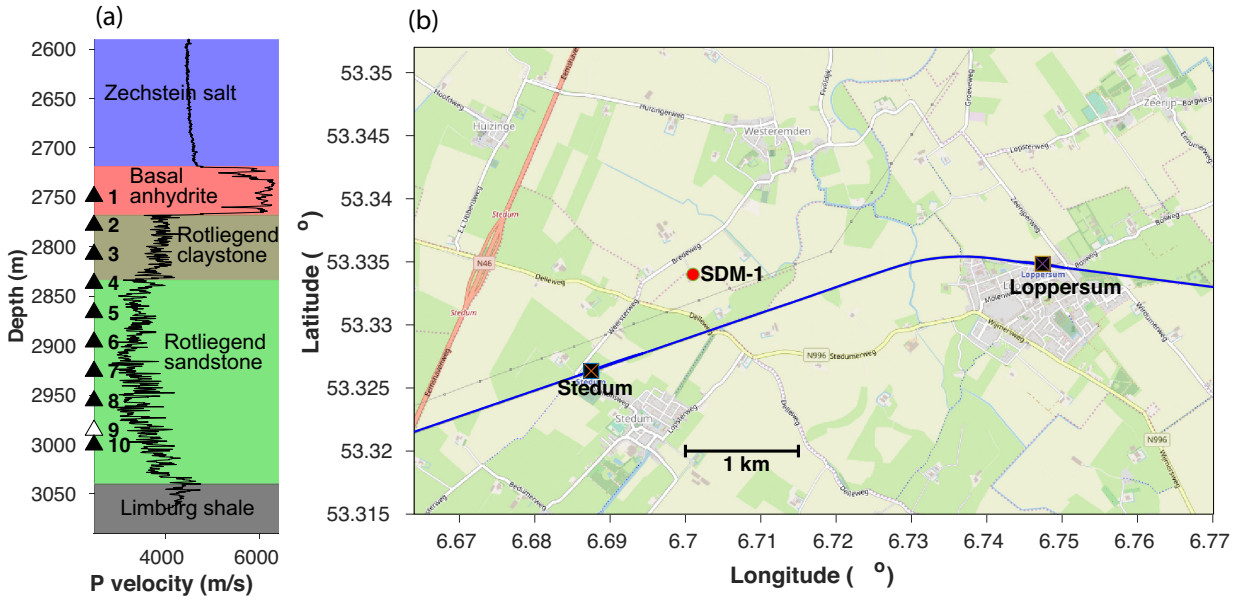

Figure 2. (a) Geophone depths (triangles), *P*-wave velocity from well-log data (black line) and lithology of borehole SDM-1. (b) Location of borehole SDM-1 and the railway track with stations Stedum and Loppersum (thick blue line).

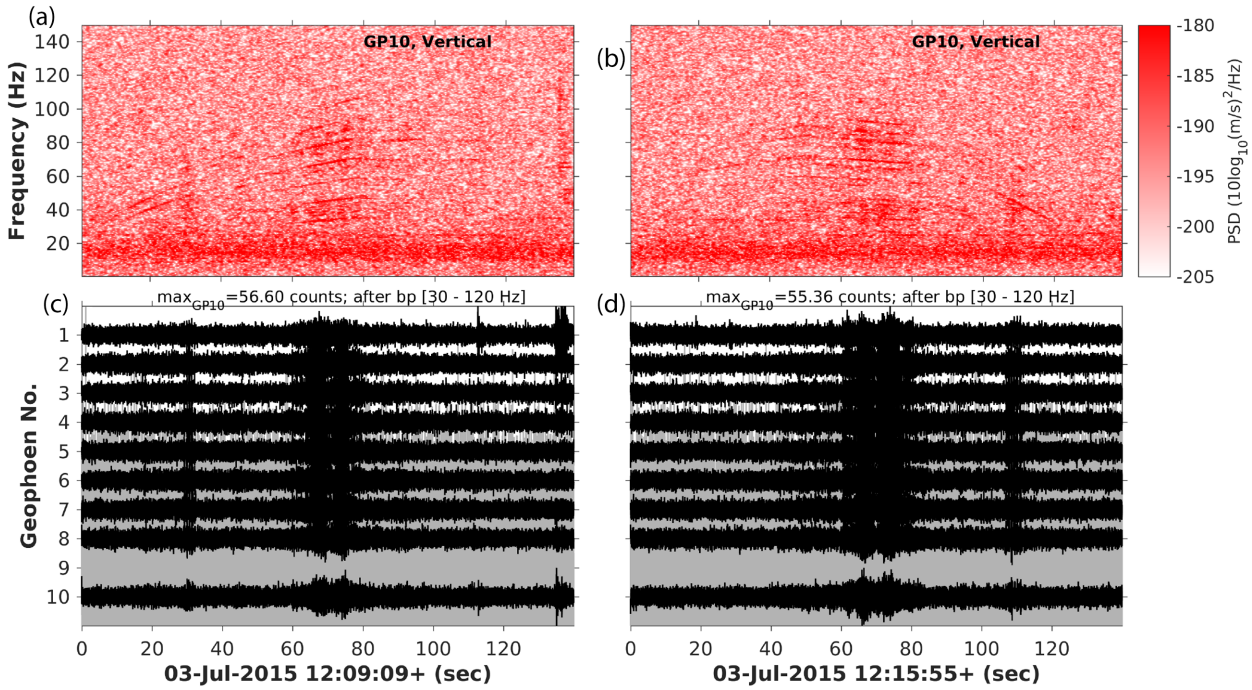

Figure 3. (a–b) Spectrograms of the recordings by geophone 10. (c–d) Filtered (30–120 Hz) vertical component geophone recordings of a train departing from Stedum station to Loppersum (c), and a train approaching Stedum station from Loppersum (d). The vertical component of geophone 9 was out of order during this deployment.

(Fig. 3c) and the next train traveling in the opposite direction (Fig. 3d). The spectrograms of the bottom geophone (GP10) are shown in Figs 3(a) and (b). Despite the large depth of the geophone array (3 km), train signals can be clearly distinguished in the spectrograms (Figs 3a and b). In the time domain, the signals can not be recognized in the unfiltered data, but they can be identified after bandpass filtering between 30 and 120 Hz (Figs 3c and d). The spectrogram of Fig. 3(a) shows that the characteristic frequencies increase from ∼20 to ∼80 s (after 12:09:09 on July 3, 2015) with maximum amplitudes between 60 and 80 s when the train is close to the borehole. The timing fits the train schedule which says that trains in the direction to Loppersum should depart from Stedum station at 12:08. The increasing frequencies are likely produced by train acceleration. Note that preceding the dominant wavetrain, there is a smaller amplitude signal at ∼30 s in Figs 3(a) and (c). The spectrogram of the next train is shown in Fig. 3(b) (starting at 12:15:55). In this case the dominant signal begins with high frequencies which gradually decrease, probably due to the deceleration

of the train approaching Stedum. The timing agrees with the train schedule: trains from Loppersum should arrive at Stedum at 12:17. The secondary arrival is now observed after the dominant train signal, at ∼110 s in Fig. 3(b). The timing of the secondary wave trains with respect to the dominant signal for trains in opposite directions suggests excitation approximately halfway between Stedum station and borehole SDM-1. A satellite image shows that there is a switch at this location from the single track to the double track at Stedum station, which likely excites the secondary arrivals. Two additional figures are presented in the supplementary material to demonstrate the similarity of the recorded train signals.

3 TRAIN SIGNAL DETECTION AND DECONVOLUTION

Unlike previous studies which used trains signals buried in continuous noise (Quiros *et al.* 2016; Brenguier *et al.* 2019; Zhang *et al.* 2019), we use isolated train signals to exclude other types of noise and signals. This requires identification and extraction of the train signals from the continuous noise data.

The train signals have the character of a wave train without a clear onset, their amplitude is slightly higher than the noise level in the 30–120 Hz frequency band and their duration is up to 100 s (Fig. 3). A first quick-and-dirty detection is obtained from the 30 to 120 Hz continuous, vertical component data of geophone 2: the average of the (absolute) amplitude of a 30 s moving time window should be higher than a threshold which is just above noise level. Then, the spectrogram around each potential event is obtained. For each spectrum (as a function of time) the total power within the 30–90 Hz frequency band is calculated. This time-dependent signal is then smoothed to allow clear identification of the main and the secondary train signals (their time difference is normally 30–40 s, see Fig. 3). When the secondary signal arrives before the dominant signal, the event is identified as a train from Stedum to Loppersum, if the order is reversed it is identified as a train in the opposite direction. In this way, out of the roughly 9000 detected trains for each 5-month period, the travel direction of approximately 7000 trains could be determined. Finally, a 20 s time window is determined around the maximum of the main signal. The choice of 20 s is based on the observation that the dominant signal often has this duration (from 60 to 80 s in Fig. 3).

The *P*- and *S*-wave response can be obtained by interferometry using cross-correlation or deconvolution (Snieder *et al.* 2006, 2009). Rather than applying cross-correlation as in Zhou & Paulssen (2017), deconvolution was chosen in this study because of the ability to preserve the high frequencies while eliminating the transient train time signal. Akbar *et al.* (2018) showed that the deconvolution method performs well on the geophone data of SDM-1.

In the frequency domain, the deconvolution of the *j*th component of geophone R (R^j) by the *i*th component of geophone S (S^i) is given by

$$D^{ji}_{RS}(\omega) = \frac{R^j(\omega)}{S^i(\omega)}, \tag{1}$$

where D^{ji}_{RS} may be interpreted as an estimate of the Green's function response of a virtual source at the location of S acting in the *i*-direction recorded by a receiver at the location of R in the *j*-direction. In practice, to preserve stability of the deconvolution, a water level is applied and the deconvolution is approximated by:

$$D^{ji}_{RS}(\omega) \approx \frac{R^j(\omega)S^{i*}(\omega)}{\Phi^i(\omega)}, \tag{2}$$

where $S^{i*}(\omega)$ is the complex conjugate of $S^i(\omega)$, and $\Phi^i(\omega)$ is its autocorrelation with a water level:

$$\Phi^i(\omega) = \max\left\{S^i(\omega)S^{i*}(\omega),\ c\cdot\max\{S^i(\omega)S^{i*}(\omega)\}\right\}. \tag{3}$$

The water level is taken as 0.01 per cent of the maximum spectral power of the autocorrelation ($c = 0.0001$). If the autocorrelation for a certain frequency has a value below this water level it is replaced by it. As train signals are strongest in the 30–90 Hz frequency band (Figs 3a and b). The deconvolutions are calculated for 30–90 Hz bandpass filtered data to avoid influence from the higher amplitude noise at frequencies below 30 Hz.

4 *P*- AND *S*-WAVE RESPONSE OF THE RESERVOIR

We retrieved *P*- and *S*-wave responses from the intergeophone deconvolutions. The *P*-wave responses are obtained from the vertical component deconvolutions, as the *P* wave predominantly propagates in the vertical direction along the deep geophone array. In the following, we illustrate the method for the data of the second deployment (July 3–December 1, 2015). Fig. 4(b) presents the vertical component deconvolutions of a single train using the signal of the top geophone [$D^{ZZ}_{RS}(t)$, with S = GP01 and R = GP01–GP10]. It shows that a stable deconvolution response is already obtained for a single train signal. The direct downgoing *P* wave from GP01 is retrieved robustly, despite the slight oscillations that are present after the main peak. By averaging over 60 trains (approximately the number of identified trains per day), we obtained stable deconvolutions that are nearly identical to the ∼9000-train average for the entire deployment period (Fig. 4c). By stacking, incoherent oscillations are significantly reduced and reflections from the bottom and the top of the reservoir can be distinguished. Although the *P* wave coda is determined with sufficient accuracy to allow a more detailed investigation, we focus here on the direct *P* wave because it has a higher amplitude and is more stable.

Other train noise interferometric studies retrieved *P* or Rayleigh wave responses (Quiros *et al.* 2016; Brenguier *et al.* 2019; Zhou & Paulssen 2019). Here we show that the *S*-wave response can also be obtained from train signals. To obtain the *S*-wave response with the highest signal-to-noise ratio, we searched for the direction that gives strongest *S*-wave amplitude. To find this direction, we performed horizontal component deconvolutions for all azimuths for the geophone pair GP02–GP10, covering the largest distance in the reservoir. The horizontal component pairs were rotated from west (–90°) to east (90°) to find the largest amplitude. Fig. 5 shows that the largest amplitude is obtained at approximately 0.11 s for an azimuth of –35° or, alternatively, 145°. The timing matches the expected *S*-wave traveltime for the velocity model of Zhou & Paulssen (2017). Considering the uncertainty in the observed azimuth, the uncertainty in the orientations of the horizontal components (±15°), as well as the fact that the trains are moving sources, it is likely that the azimuth of –35° roughly agrees with the direction from SDM-1 to the dominant source direction. If the *S* waves were excited by the horizontal movement of the train on the railway track, the maximum *S*-wave polarization is expected to be roughly parallel to the railway (the frictional forces would excite horizontal shear displacements parallel to the track). Instead, the obtained direction is roughly perpendicular, corresponding to the source–receiver direction, that is within the vertical plane of dominant wave propagation. With the polarization in this plane it is likely that the recorded *S* waves are *SV* waves generated by conversion from *P* waves in the overburden

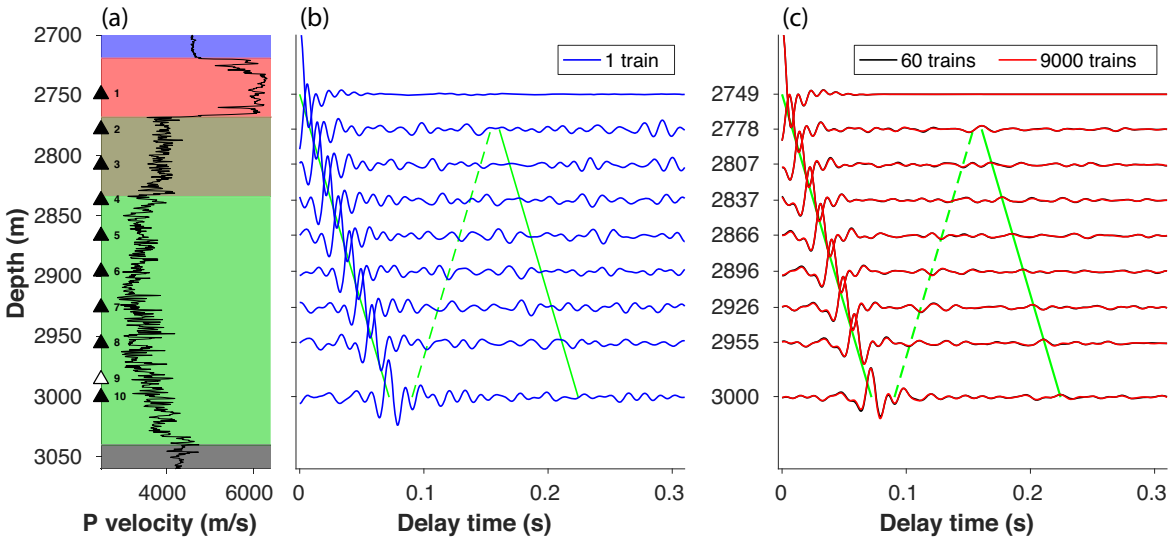

Figure 4. (a) Geophone depths (similar to Fig. 2a). (b) Vertical component deconvolutions for a single train using the data of the top geophone. (c) Stacked deconvolutions for 60 trains (black) and 9000 trains (red, on top). Solid and dashed green lines represent the predicted down- and upgoing reflected *P* waves for an average reservoir velocity of 3500 m s^{-1} based on sonic log data provided by NAM.

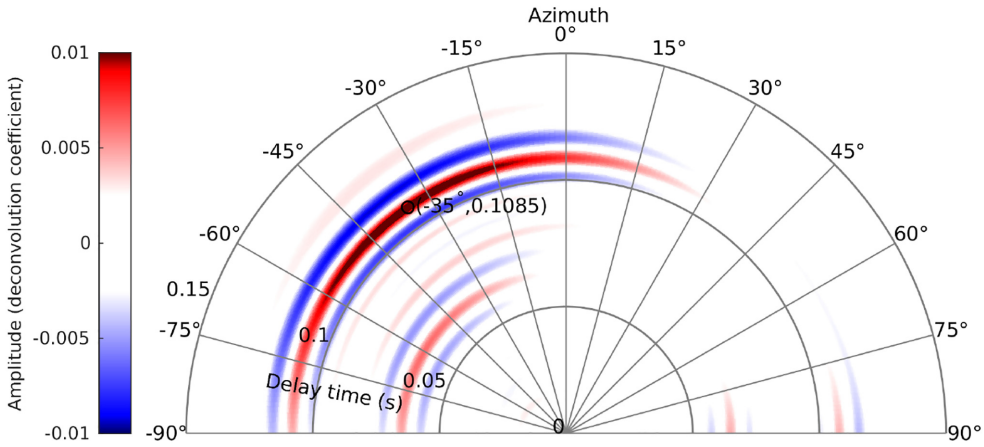

Figure 5. Horizontal component deconvolutions of geophone 10 with geophone 2 as a function of azimuth. The time axis ranges from 0 to 0.15 s in the radial direction. The largest amplitude is found for an azimuth of –35° at 0.108 s, corresponding to the intergeophone *S* wave traveltime.

of the reservoir. Because the relative orientations of the horizontal components with respect to each other are fairly well constrained (Zhou 2020), the horizontal components of all geophones were rotated to 145° and 55°. We found that the train signal deconvolutions between the geophone pairs for the 145° direction indeed produced clear *S*-wave responses. Fig. 6(b) shows that the downgoing direct *S* wave, with an average velocity of 2100 m s^{-1}, can be obtained from a single train deconvolution. Similar to the *P*-wave response, the *S*-wave stack of 60 trains gives nearly identical results to the one of ∼9000 trains (Fig. 6c), although the *S*-wave response is smaller in amplitude compared to the *P*-wave response.

5 *P*- AND *S*-WAVE VELOCITY IN THE RESERVOIR

The previous section showed that intergeophone *P*- and *S*-wave responses can be retrieved from deconvolutions of individual train signals. Thus, the *P* and *S* wave traveltimes for all possible geophone pairs can be measured from the peaks of the downgoing direct waves. The velocity structure can then be calculated from the traveltime data. Similar to Zhou & Paulssen (2017), a kernel density estimation (Botev *et al.* 2010) is used to obtain the probability density function of the measured traveltimes for each geophone pair and its maximum likelihood value is taken as the intergeophone traveltime. The traveltimes from all geophone combinations are then used in a linear least squares inversion to obtain the *P* and *S* wave traveltimes between neighbouring geophones with uncertainty. Subsequently, the *P*- and *S*-wave velocity profiles are calculated. Fig. 7 presents the *P*- and *S*-velocity profiles obtained from the two data sets for 2015. We note that the uncertainty in the *P*-velocity profile is very small with a maximum value of 20 m s^{-1} (0.4 per cent). The uncertainty in the *S*-velocity profile is somewhat larger, varying between 30 and 80 m s^{-1} (1–3 per cent). The small uncertainties illustrate the high accuracy of the traveltime measurements and their internal consistency. Furthermore, we investigated the difference in the *P* velocity profiles calculated for trains traveling in the two opposite directions and found this difference to be negligible, that is, overlapping within the uncertainty (see also Zhou & Paulssen 2019).

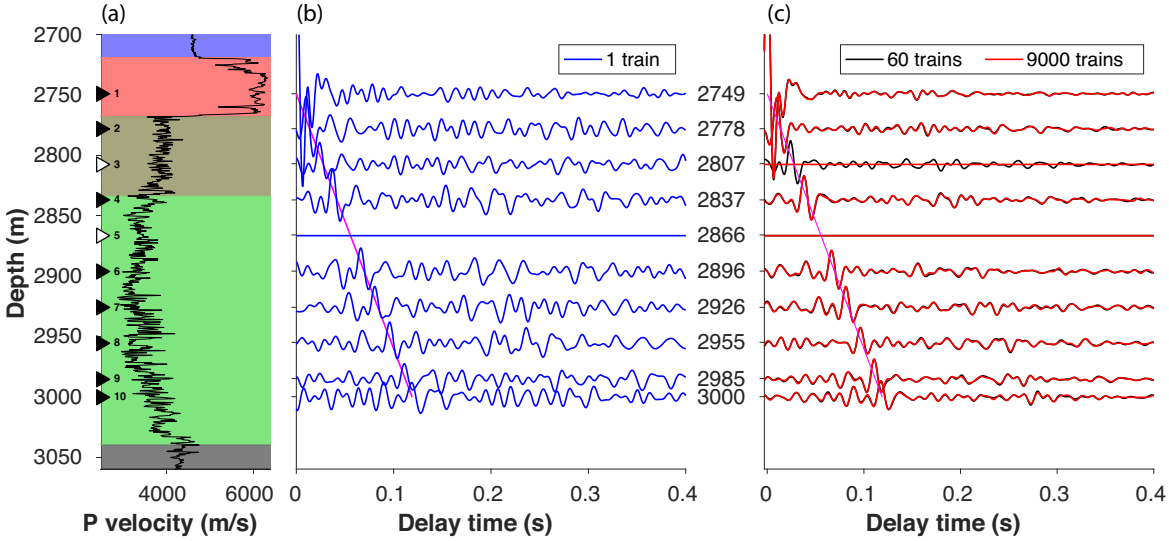

Figure 6. (a) Geophone depths and lithology as in Fig. 4(a). (b) Horizontal component deconvolutions for a single train for an azimuth of 145°. (c) Stacked deconvolutions for 60 trains (black) and ∼ 9000 trains (red, on top). The magenta line indicates a downgoing *S* wave with a velocity of 2100 m s^{-1} (Geophone 5 had one horizontal component out of order. Geophone 3 was working in the beginning but broke down after 10 d).

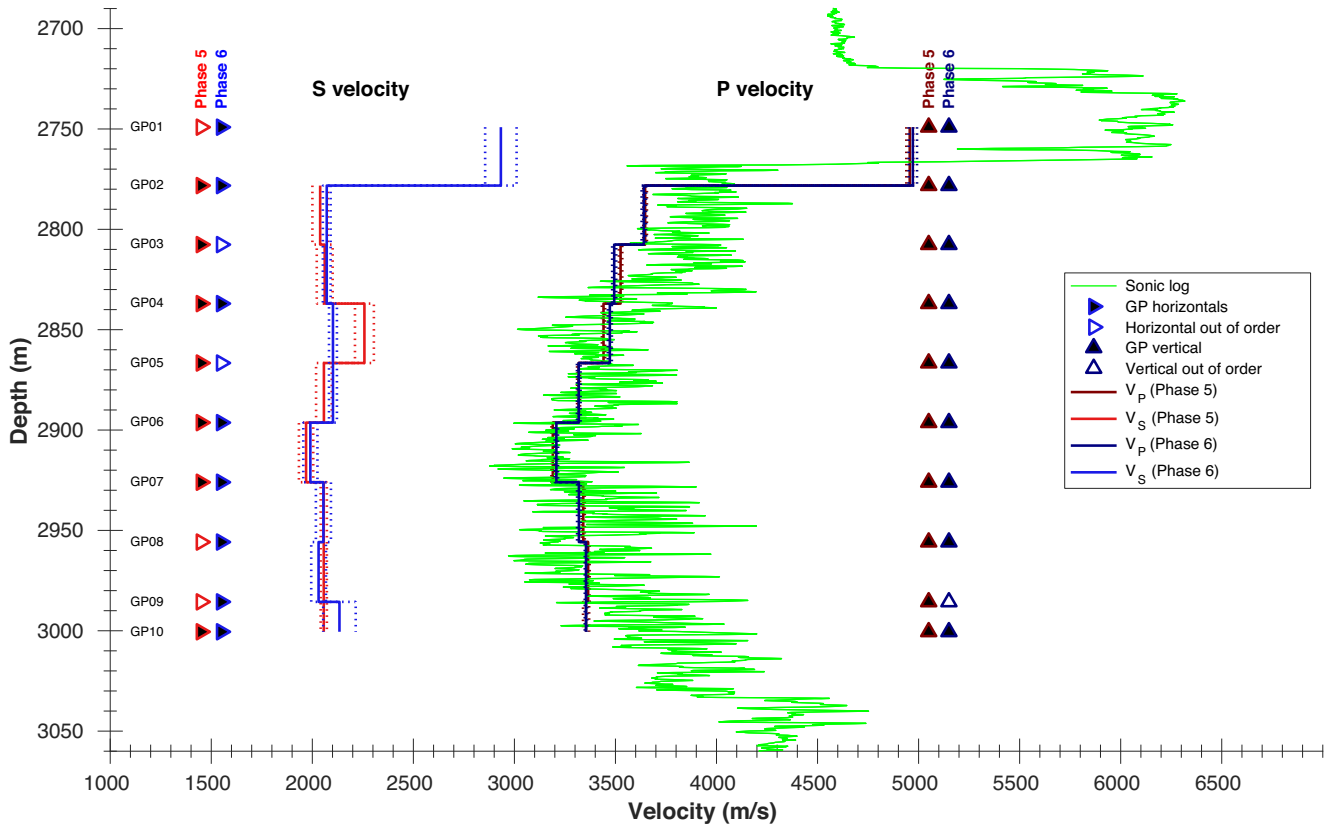

Figure 7. *P*- and *S*-velocity profiles (solid) by train-signal deconvolution obtained for the two deployments: January 23–June 29, 2015 ('phase 5', red) and July 3–December 1, 2015 ('phase 6', blue). The errors are indicated by the dashed lines. Triangles represent geophone positions: filled when the components were operational during the entire deployment (left for horizontals, right for vertical). The sonic log in green is provided by NAM.

The *P*-velocity structure obtained by train noise interferometry matches the sonic log data provided by NAM very well demonstrating the suitability of the approach and the accuracy of the results. However, we observe that our average *P*-wave velocity for the Ten Boer claystone (the interval between GP02 and GP04) is lower than the sonic log measured in 1963. This was also found in our previous study which used ambient noise cross-correlations (Zhou & Paulssen 2017), but the uncertainty in the current study is much smaller. The cause of the smaller *P* velocity in the claystone obtained from our data compared to the sonic log data is not clear.

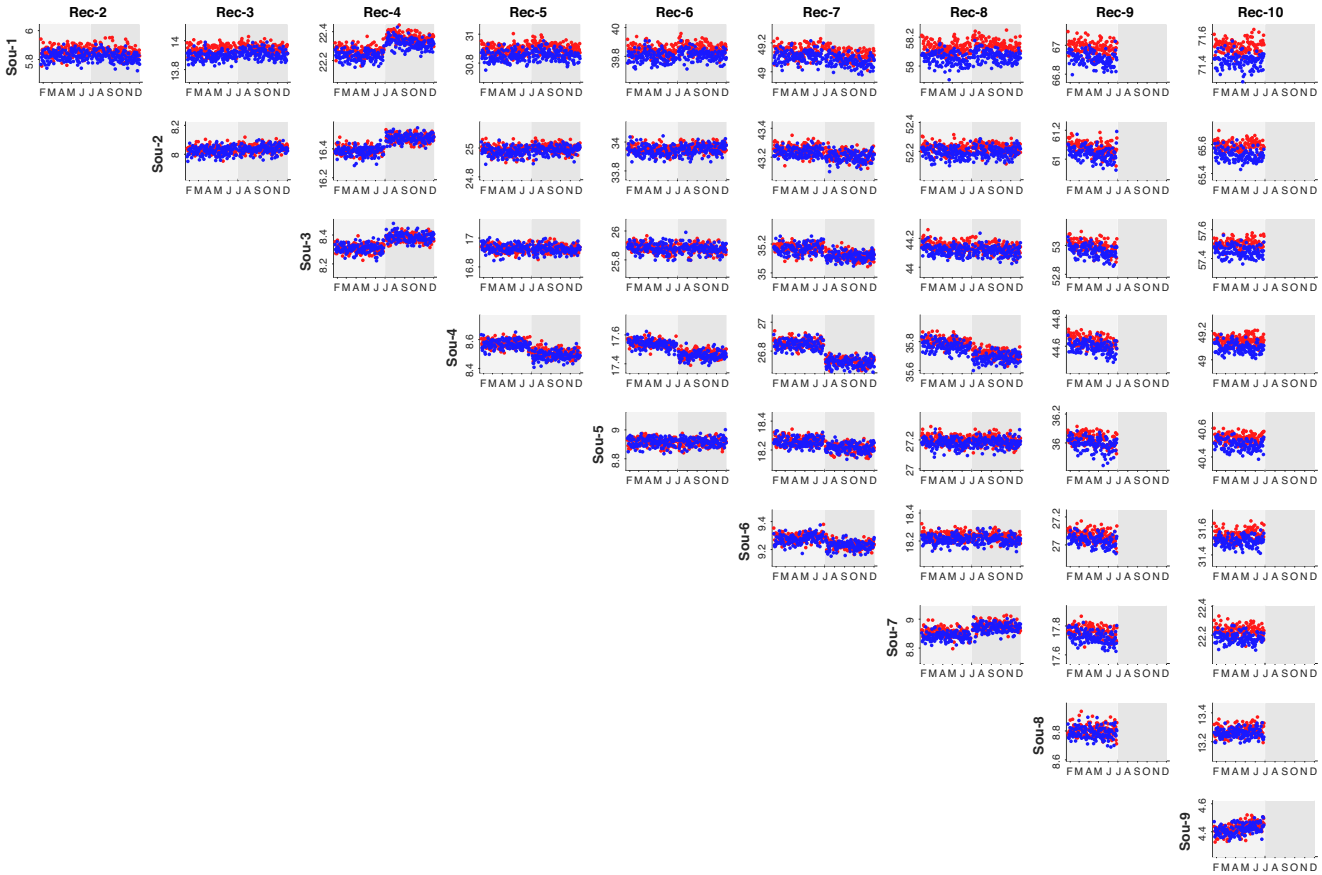

Figure 8. *P* wave traveltimes (±0.2 ms around median value are presented) as a function of time from the stacked deconvolutions for all geophone combinations. Rows show diagrams for geophones acting as virtual source, columns those for geophones acting as virtual receiver. Deployment phase 5 (23 January–29 June 2015) has a light-grey background, phase 6 (3 July–1 December 2015) is in darker grey. *P* wave traveltimes obtained for trains from Stedum to Loppersum are in blue, for Loppersum to Stedum they are in red. Traveltimes along the vertical axis are in ms.

Rather than an underestimate of the true velocity, an overestimate of the (apparent) velocity may be expected from interferometry. Such an overestimate will occur if the dominant wavefield does not propagate along the array but is incident at an inclined angle. It is also unlikely that the velocity in the claystone has decreased over the past 50 yr (for instance by the opening of cracks associated to earthquakes) because we do not observe a traveltime increase for 2015 in the time lapse data, as will be presented in the next section. Potentially, there is an effect caused by the difference in scale length. The sonic log measurements typically use a 10 kHz signal corresponding to a wavelength of ∼0.4 m, whereas our measurements have frequencies from 30 to 90 Hz corresponding to wavelengths of 40–120 m. This implies that our data are sensitive to a wide area outside the borehole. The fault map provided by NAM shows a fault with an offset of 40 m at a distance of 50 m from the borehole. We speculate that heterogeneity in the vicinity of the borehole, potentially related to faulting (and their damage zones), may explain the discrepancy between our results and the sonic log data.

The *S* velocity in the reservoir is just above 2000 m s^{-1}, which is in good agreement with the average value of 2280 m s^{-1} given by NAM for the entire Groningen reservoir (Romijn 2017). The velocity profile also agrees with the previous study by Zhou & Paulssen (2017) using east-component ambient noise the cross-correlations. The largest difference is again obtained for the formation of the Ten Boer claystone (GP02–GP04), where the current study yields a lower velocity than obtained from ambient noise. There are two effects that can play a role. The ambient noise data were obtained for lower frequencies and might therefore be more strongly affected by the overlying high velocity anhydrite layer. Secondly, there can be an effect of anisotropy. The *S*-wave anisotropy over the entire (mostly sandstone) reservoir was found to be approximately 4 per cent (Zhou & Paulssen 2017) and it may be larger in the claystone. In the presence of anisotropy, the difference in inferred *S* velocity may be caused by the difference in horizontal direction that was used for the two studies.

6 TEMPORAL CHANGES OF *P* WAVE TRAVELTIMES AND AMPLITUDES

In the previous section, we used isolated train signals to calculate intergeophone *P* and *S* wave traveltimes, and from those we calculated the velocity structure. In this section, we show that the data can also be used to determine temporal variations.

To obtain time-lapse intergeophone traveltime measurements with a higher accuracy than single trains, we stacked the deconvolutions of 30 consecutive trains travelling in the same direction. Traveltimes of the direct *P* waves are then measured from the 30-train stacks. Since there are typically about 30 identified train signals per direction per day, this approximately corresponds to one measurement per day for each direction. For the two deployments of 2015, this allows analysis of temporal variations over the year. Fig. 8 gives an overview of all *P* wave traveltime measurements. Each row shows the traveltime diagrams obtained from the stacked

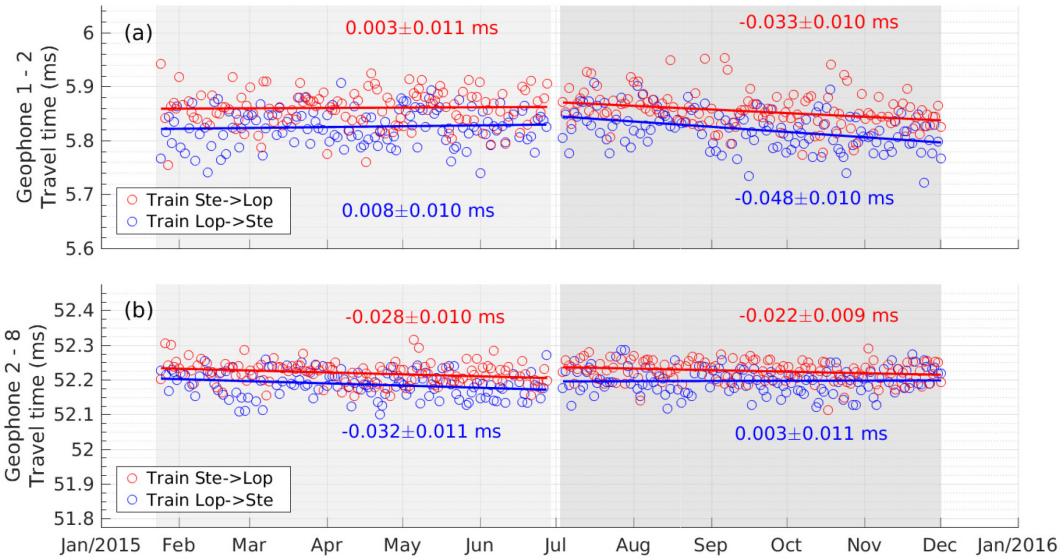

Figure 9. (a) *P*-wave traveltimes from GP01 to GP02 and (b) from GP02 to GP08. The measurements are obtained from stacked deconvolutions for trains from Stedum to Loppersum (red) and from Loppersum to Stedum (blue). The two deployments are indicated by their gray scale background. Linear fits are applied to the data and the accumulated traveltime change per deployment period (with standard deviation) is noted.

Table 1. *P* wave traveltime changes for January 23–June 29 in μs. Values for trains from Stedum to Loppersum are shown in red (top) and those for Loppersum to Stedum in blue (bottom).

	Rec01	Rec02	Rec03	Rec04	Rec05	Rec06	Rec07	Rec08	Rec09	Rec10
Sou01	–	3 ± 11	1 ± 9	−14 ± 10	−3 ± 11	−17 ± 11	−3 ± 12	−27 ± 11	−30 ± 13	−10 ± 14
		8 ± 10	11 ± 9	−4 ± 11	9 ± 11	−13 ± 12	11 ± 12	−40 ± 13	−54 ± 13	−9 ± 15
Sou02	14 ± 11	–	−7 ± 7	−6 ± 8	−5 ± 9	−29 ± 8	−5 ± 11	−28 ± 10	−57 ± 12	−5 ± 11
	7 ± 12		13 ± 9	9 ± 9	−9 ± 10	−20 ± 11	6 ± 9	−32 ± 11	−53 ± 13	−30 ± 11
Sou03	14 ± 9	4 ± 7	–	−0± 9	−15 ± 8	−38 ± 9	−7 ± 9	−34 ± 10	−70 ± 11	−3 ± 10
	−0 ± 10	6 ± 8		3 ± 9	−8 ± 9	−26 ± 11	15 ± 10	−27 ± 10	−59 ± 11	−24 ± 11
Sou04	3 ± 10	−12 ± 7	−8 ± 7	–	−2 ± 8	−25 ± 7	−9 ± 8	−22 ± 8	−65 ± 10	−4 ± 9
	1 ± 10	−1 ± 8	−8 ± 9		−9 ± 9	−34 ± 8	−2 ± 10	−24 ± 11	−47 ± 11	−17 ± 10
Sou05	4 ± 11	−13 ± 8	−13 ± 8	−2 ± 8	–	−9 ± 8	−13 ± 8	−19 ± 9	−55 ± 11	−0 ± 9
	−21 ± 12	2 ± 9	−8 ± 9	−1 ± 8		−5 ± 9	0 ± 10	−16 ± 10	−45 ± 14	−31 ± 11
Sou06	−22 ± 10	−36 ± 9	−40 ± 9	−40 ± 8	−14 ± 8	–	24 ± 9	5 ± 9	−35 ± 11	26 ± 11
	−25 ± 11	−28 ± 9	−32 ± 9	−29 ± 8	−23 ± 9		39 ± 10	−1 ± 9	−48 ± 11	5 ± 11
Sou07	14 ± 11	−10 ± 9	−4 ± 8	−11 ± 7	−11 ± 8	26 ± 9	–	−24 ± 9	−45 ± 12	−12 ± 11
	−2 ± 10	−8 ± 9	−20 ± 10	−6 ± 9	−20 ± 9	19 ± 9		2 ± 8	−63 ± 12	−13 ± 10
Sou08	−1 ± 12	−36 ± 10	−28 ± 9	−14 ± 8	−31 ± 9	−1 ± 9	−13 ± 9	–	0 ± 12	30 ± 11
	−64 ± 13	−36 ± 9	−39 ± 9	−28 ± 10	−24 ± 9	−17 ± 9	−6 ± 9		−9 ± 12	6 ± 10
Sou09	−5 ± 14	−44 ± 10	−63 ± 11	−47 ± 11	−40 ± 10	−30 ± 12	−51 ± 12	−5 ± 11	–	69 ± 11
	−10 ± 17	−39 ± 9	−52 ± 10	−32 ± 11	−24 ± 12	−16 ± 12	−45 ± 10	3 ± 11		51 ± 10
Sou10	17 ± 15	−3 ± 11	−10 ± 11	−7 ± 10	−12 ± 10	26 ± 11	12 ± 12	32 ± 12	73 ± 10	–
	−10 ± 16	−33 ± 11	−39 ± 10	−18 ± 10	−32 ± 10	2 ± 12	−41 ± 11	−0 ± 10	45 ± 11	

vertical-component deconvolutions with, from top to bottom, the signal of geophone GP01–GP09 (i.e. the denominator in the frequency representation of the deconvolution). These geophones can be interpreted as the virtual sources. The columns represent the virtual receivers, the signal which is deconvolved. Within each diagram, the background indicates the deployment period: light grey for January 23–June 29 and darker grey for July 3–December 1. The traveltime measurements for trains from Stedum to Loppersum are in blue and those for the opposite direction are in red. There are no data for GP09 for the second deployment because the vertical component was out of order. Furthermore, the data of GP10 are affected by a change in the level of the gas–water contact related to drilling activities during the second deployment (Zhou 2020) and are therefore not shown.

Some diagrams show distinct steps in traveltime from the first deployment to the next, for instance for the geophone pairs that have GP04 as virtual source or receiver. These are likely caused by small changes in geophone position between the two deployments. To investigate the long-term traveltime changes that might be related to reservoir compaction, we applied linear fits to the traveltime data. We did this per deployment period for each geophone pair and obtained independent estimates for trains from Stedum to Loppersum and the opposite direction. The traveltime changes over the entire deployment period are then estimated from the linear fits. Fig. 9 shows examples for the geophone pair GP01 → GP02 across the anhydrite–claystone interface (Fig. 9a) and for geophone pair GP02 → GP08 along the reservoir (Fig. 9b). Compilations of all traveltime changes per 5-month deployment period are presented in Tables 1 and 2. To assess the reliability of the results, we not only calculated the traveltime changes for the deconvolutions with the virtual source above the virtual receiver (data above the diagonal in Tables 1 and 2), but also for the virtual source below the virtual receiver (data below the diagonal). It can be verified that most of the measurements are in agreement within the error. The tables show that most intergeophone traveltimes decreased a few or a few tens of microseconds per 5-month deployment period. The 1-standard deviation uncertainties are typically around 10 μs. Since the traveltime changes are generally smaller or just slightly bigger than the

Table 2. *P* wave traveltime changes for July 3–December 1 in microseconds. Values for trains from Stedum to Loppersum are shown in red at the top and those for Loppersum to Stedum in blue at the bottom.

	Rec01	Rec02	Rec03	Rec04	Rec05	Rec06	Rec07	Rec08
Sou01	–	-33 ± 10	-26 ± 8	-28 ± 9	-37 ± 10	-31 ± 10	-47 ± 10	-53 ± 11
		-48 ± 10	-33 ± 9	-41 ± 10	-38 ± 10	-38 ± 10	-44 ± 11	-39 ± 11
Sou02	-33 ± 9	–	8 ± 8	-6 ± 8	-14 ± 8	-5 ± 8	-14 ± 10	-22 ± 9
	-56 ± 11		9 ± 8	4 ± 8	8 ± 8	23 ± 10	-0 ± 10	3 ± 11
Sou03	-27 ± 10	-3 ± 7	–	-8 ± 8	-7 ± 8	-23 ± 9	-15 ± 9	-30 ± 9
	-41 ± 11	5 ± 8		-11 ± 9	-7 ± 8	-7 ± 9	8 ± 8	-16 ± 10
Sou04	-14 ± 10	-5 ± 7	-11 ± 8	–	-11 ± 8	-7 ± 8	-12 ± 7	-30 ± 8
	-67 ± 12	-14 ± 7	-21 ± 9		6 ± 9	12 ± 8	1 ± 10	20 ± 10
Sou05	-44 ± 10	-24 ± 7	-11 ± 7	-2 ± 9	–	4 ± 8	-13 ± 9	-23 ± 10
	-54 ± 12	6 ± 9	-2 ± 8	-8 ± 9		-1 ± 8	-6 ± 9	-13 ± 9
Sou06	-29 ± 9	-11 ± 8	0 ± 8	4 ± 8	1 ± 8	–	-9 ± 8	-15 ± 8
	-32 ± 11	26 ± 9	5 ± 8	7 ± 9	7 ± 8		-8 ± 9	-17 ± 9
Sou07	-17 ± 11	-4 ± 9	-10 ± 8	3 ± 8	6 ± 8	-10 ± 9	–	-6 ± 9
	-67 ± 14	6 ± 9	-12 ± 9	3 ± 8	-2 ± 9	-21 ± 8		-6 ± 9
Sou08	-41 ± 12	-29 ± 9	-24 ± 9	-16 ± 9	-19 ± 9	-22 ± 8	-14 ± 8	–
	-48 ± 14	15 ± 11	-8 ± 10	5 ± 10	-1 ± 10	-17 ± 10	11 ± 9	

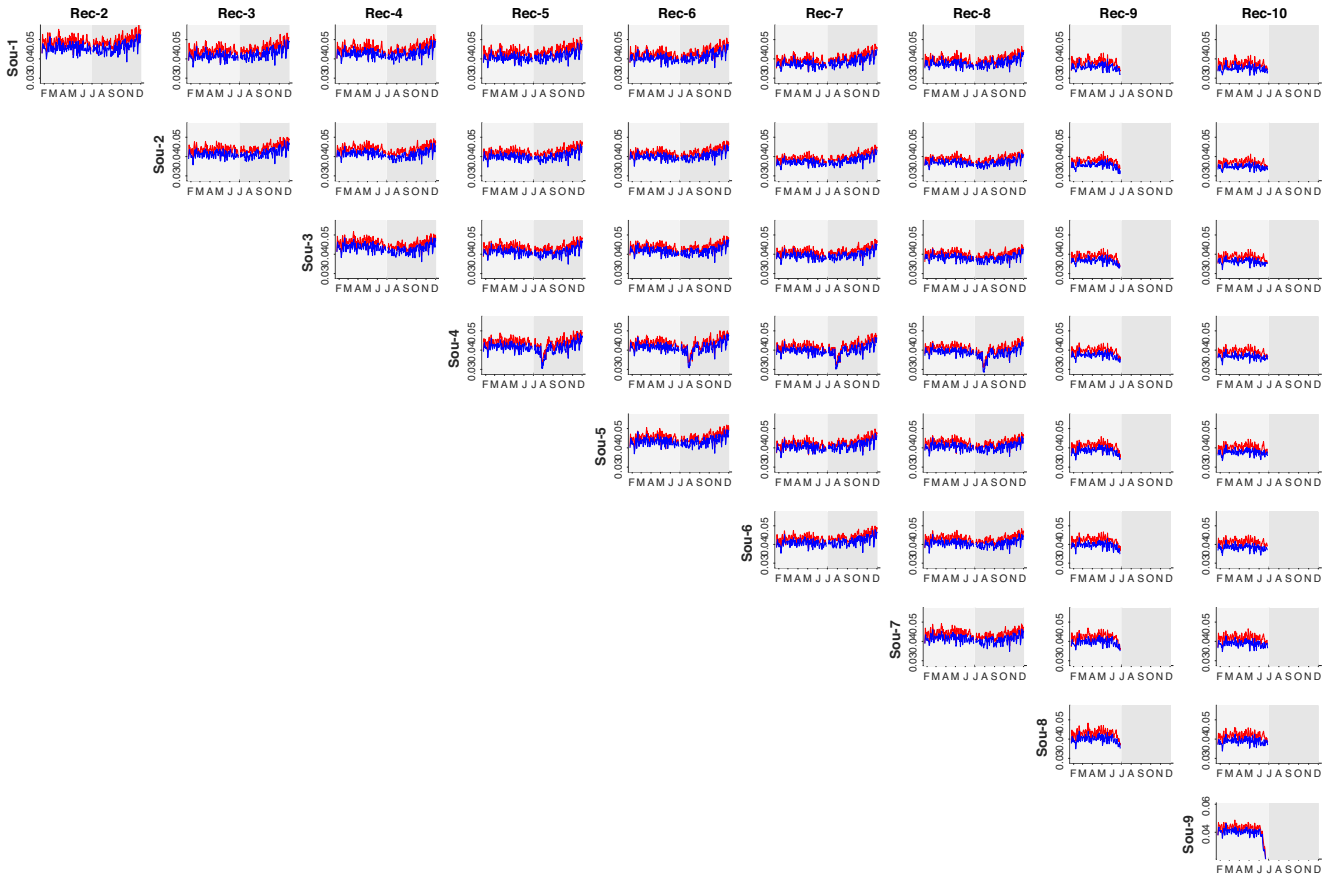

Figure 10. Amplitude measurements of the direct *P* wave from the stacked deconvolutions as a function of time. Rows show diagrams with geophones acting as virtual source, columns those for geophones acting as virtual receiver. Deployment phase 5 (23 January–29 June 2015) has a light-grey background, phase 6 (3 July–1 December 2015) is in darker grey. Amplitudes obtained for trains from Stedum to Loppersum are in blue, for Loppersum to Stedum they are in red.

uncertainty, it is difficult to draw hard conclusions. However, the general pattern of decreasing traveltimes (negative values in Tables 1 and 2) is in agreement with an increase in velocity caused by compaction.

We note that our temporal traveltime changes of up to tens of microseconds per 5-month period are much smaller than the traveltime changes that are typically obtained for time-lapse 3-D seismic surveys. These vary between 0.1 and 1.5 ms yr^{-1} for various sandstone reservoirs, although reservoir slowdown has also been observed (MacBeth *et al.* 2019). We point out that the traveltimes changes of the two methods can not be directly compared. The active time-lapse seismic surveys include the effects of strain, that is reservoir thinning (or possibly extension), as well as of changes in medium velocity. The traveltimes measured by our interferometric approach, on the other hand, are obtained relative to fixed geophone positions within the borehole. They do not include changes in layer thickness and only reflect velocity variations in the medium.

Compaction may also affect the amplitudes of the deconvolutions. Deconvolution interferometry largely eliminates the source signal, so when the noise sources are repetitive and stable, amplitude variations of the deconvolutions can reflect changes in the medium. The (maximum) amplitude of the direct *P* wave was measured from the stacked train deconvolutions. An overview of all the data is presented in Fig. 10. Generally, there are only small amplitude variations during the first half of 2015, whereas all geophone combinations show a gradual amplitude increase during the second half of 2015. During this period, the amplitude typically increases from ∼0.04 to ∼0.045, corresponding to a 12 per cent increase. It might be tempting to explain the amplitude increase by compaction, but the absence of such a trend during the first half of 2015 suggests that this interpretation is not warranted.

7 CONCLUSIONS

This study shows that it is feasible to very accurately determine direct *P* and *S* wave traveltimes along a geophone array by deconvolution interferometry of train signals. The study was carried out for a deep borehole geophone array in the Groningen gas reservoir to investigate effects of compaction. Intergeophone traveltimes measured from isolated train signals were first used to determine the velocity structure along the geophone array. The *P* velocity profile, retrieved from vertical component deconvolutions, was found to be in good agreement with sonic log data except for the Ten Boer claystone layer in the reservoir. There, our data yield a roughly 10 per cent smaller velocity than the sonic log, clearly exceeding the 0.4 per cent *P* velocity uncertainty estimated from the train data. The discrepancy can be caused by the difference in scale length of more than a factor of 100 between the sonic log data and our train signal data, and may reflect non-homogeneous structure around the borehole. The *S* velocity structure was inferred from horizontal component train signal deconvolutions. The *S* waves have maximum amplitude in the direction perpendicular to railway, suggestive of an SV wavefield generated by *P*-to-*S* conversions at lithological interfaces between the surface and the geophone array. The *S* velocity model from train signals is in good agreement with that obtained from a previous study using ambient noise cross-correlation interferometry (Zhou & Paulssen 2017) with the largest difference again for the claystone layer of the reservoir. Yet, we find that the *S*-velocity models are overall in good agreement considering the uncertainties in the previous study as well as potential effects of anisotropy (∼4 per cent, see Zhou & Paulssen 2017).

The train signal deconvolutions were then used to investigate temporal variations of the *P*-wave response. Most of the (daily stacked) intergeophone *P* wave traveltimes showed a slightly negative trend for the two 5-month deployments in 2015. Whereas this is in line with an interpretation of reservoir compaction increasing the *P*-wave velocity, many of the intergeophone traveltime changes were too small to be significant considering the uncertainties. It is noteworthy that the changes, which are up to several tens of microseconds per 5-month period, are smaller than obtained by time-lapse 3-D seismic surveys for a large variety of reservoirs. Our interferometric approach is only sensitive to variations in medium velocity (assuming that the geophones within the steel casing of the borehole do not move along with the surrounding rock), whereas the traveltime changes from the time-lapse seismic surveys include the additional effect of changes in reservoir thickness. The *P*-wave amplitude data of the deconvolutions also did not show clear evidence for compaction. The amplitudes consistently increased during the second deployment, as expected for compaction, but this was not observed for the first deployment. Thus, no unambiguous effects of compaction in the Groningen gas reservoir were found for the two 5-month deployments analysed in this study. Nevertheless, our results demonstrate that very small temporal changes in the medium can be detected by train noise interferometry applied to borehole geophone array data.

ACKNOWLEDGEMENTS

We thank NAM for providing us with the data. Chris Spiers, André Niemeijer, Jianye Chen, Ivan Vasconcelos and Elmer Ruigrok are thanked for useful discussions. We thank Augusto Casas and an anonymous reviewer for their constructive comments that helped to improve the paper. Base map in Fig. 2(b) is retreived from OpenStreetMap. This project has been funded by the European Union's Horizon 2020 research and innovation program under the Marie Skłodowska-Curie actions grant agreement No 642029 - ITN CREEP.

REFERENCES

Akbar, M., Vasconcelos, I., Zhou, W. & Paulssen, H., 2018. Subsurface reflection response estimation at Groningen by seismic interferometry using deep borehole data, in *Extended Abstract of 80th EAGE Conference and Exhibition 2018,* Vol. 2018, pp. 1–5, European Association of Geoscientists & Engineers.

Behm, M., 2017. Feasibility of borehole ambient noise interferometry for permanent reservoir monitoring, *Geophys. Prospect.,* **65,** 563–580.

Boait, F.C., White, N.J., Bickle, M.J., Chadwick, R.A., Neufeld, J.A. & Huppert, H.E., 2012. Spatial and temporal evolution of injected CO_2 at the Sleipner Field, North Sea, *J. geophys. Res.,* **117**(B3), doi:10.1029/2011JB008603.

Botev, Z.I. *et al.*, 2010. Kernel density estimation via diffusion, *Ann. Stat.,* **38**(5), 2916–2957.

Bourne, S., Oates, S., Van Elk, J. & Doornhof, D., 2014. A seismological model for earthquakes induced by fluid extraction from a subsurface reservoir, *J. geophys. Res.,* **119**(12), 8991–9015.

Brenguier, F., Campillo, M., Hadziioannou, C., Shapiro, N., Nadeau, R.M. & Larose, E., 2008. Postseismic relaxation along the San Andreas fault at Parkfield from continuous seismological observations, *Science,* **321**(5895), 1478–1481.

Brenguier, F. *et al.*, 2019. Train traffic as a powerful noise source for monitoring active faults with seismic interferometry, *Geophys. Res. Lett.,* **46**(16), 9529–9536.

Brenguier, F. *et al.*, 2020. Noise-based ballistic wave passive seismic monitoring. Part 1: body waves, *J. geophys. Int.,* **221**(1), 683–691.

Candela, T., Wassing, B., ter Heege, J. & Buijze, L., 2018. How earthquakes are induced, *Science,* **360**(6389), 598–600.

Cannon, M. & Kole, P., 2018. The first year of distributed strain sensing (DSS) monitoring in the Groningen gas field, Report No. SR.17.009342, Nederlands Aardolie Maatschappij .

Chen, Q.-F., Li, L., Li, G., Chen, L., Peng, W., Tang, Y., Chen, Y. & Wang, F., 2004. Seismic features of vibration induced by train, *Acta Seismol. Sin.,* **17**(6), 715–724.

Fuchs, F. & Bokelmann, G., 2018. Equidistant spectral lines in train vibrations, *Seismol. Res. Lett.,* **89**(1), 56–66.

Hatchell, P. & Bourne, S., 2005. Rocks under strain: Strain-induced time-lapse time shifts are observed for depleting reservoirs, *Leading Edge,* **24**(12), 1222–1225.

KNMI, 2020. Aardbevingscatalogus of Het Koninklijk Nederlands Meteorologisch Instituut, De Bilt, The Netherlands., Available at https://www.knmi.nl/kennis-en-datacentrum/dataset/aardbevingscatalogus.

Kole, P., 2015. In-situ compaction measurements using gamma ray markers, Report No. EP201506209302, Nederlands Aardolie Maatschappij.

Larose, E., Planes, T., Rossetto, V. & Margerin, L., 2010. Locating a small change in a multiple scattering environment, *Appl. Phys. Lett.,* **96**(20), doi:10.1063/1.3431269.

MacBeth, C., Kudarova, A. & Hatchell, P., 2018. A semi-empirical model of strain sensitivity for 4D seismic interpretation, *Geophys. Prospect.,* **66**(7), 1327–1348.

MacBeth, C., Mangriotis, M.-D. & Amini, H., 2019. Post-stack 4D seismic time-shifts: interpretation and evaluation, *Geophys. Prospect.,* **67**(1), 3–31.

Mordret, A. *et al.*, 2020. Noise-based ballistic wave passive seismic monitoring. Part 2: surface waves, *J. geophys. Int.,* **221**(1), 692–705

Nakata, N. & Snieder, R., 2011. Near-surface weakening in Japan after the 2011 Tohoku-Oki earthquake, *Geophys. Res. Lett.,* **38**(17), 1–5.

Nakata, N., Snieder, R., Kuroda, S., Ito, S., Aizawa, T. & Kunimi, T., 2013. Monitoring a building using deconvolution interferometry. I: earthquake-data analysis, *Bull. seism. Soc. Am.,* **103**(3), 1662–1678.

NAM, 2018. Assessment of subsidence based on production scenario "Basispad Kabinet", Nederlands Aardolie Maatschappij.

NAM, 2020. NAM interactieve kaart of the Nederlands Aardolie Maatschappij, Assen, The Netherlands, Available at https://nam-feitenencijfers.data-app.nl/geotool/nam.html.

Niu, F., Silver, P., Daley, T., Cheng, X. & Majer, E., 2008. Preseismic velocity changes observed from active source monitoring at the Parkfield SAFOD drill site, *Nature,* **454**(7201), 204–208.

Obermann, A., Planès, T., Larose, E. & Campillo, M., 2019. 4-D Imaging of subsurface changes with coda waves: numerical studies of 3-D combined sensitivity kernels and applications to the Mw 7.9, 2008 Wenchuan earthquake, *Pure appl. Geophys.,* **176**(3), 1243–1254.

Pei, S., Niu, F., Ben-Zion, Y., Sun, Q., Liu, Y., Xue, X., Su, J. & Shao, Z., 2019. Seismic velocity reduction and accelerated recovery due to earthquakes on the Longmenshan fault, *Nat. Geosci.,* **12**(5), 387–392.

Pijnenburg, R., Verberne, B., Hangx, S. & Spiers, C., 2018. Deformation behavior of sandstones from the seismogenic Groningen gas field: role of inelastic versus elastic mechanisms, *J. geophys. Res.,* **123**(7), 5532–5558.

Pijnenburg, R., Verberne, B., Hangx, S. & Spiers, C., 2019. Inelastic deformation of the Slochteren sandstone: stress-strain relations and implications for induced seismicity in the Groningen gas field, *J. geophys. Res.,* **124**(5), 5254–5282.

Quiros, D.A., Brown, L.D. & Kim, D., 2016. Seismic interferometry of railroad induced ground motions: body and surface wave imaging, *J. geophys. Int.,* **205**(1), 301–313.

Romijn, R., 2017. Groningen velocity model 2017 - Groningen full elastic velocity model, Nederlands Aardolie Maatschappij.

Salvermoser, J., Hadziioannou, C. & Stähler, S.C., 2015. Structural monitoring of a highway bridge using passive noise recordings from street traffic, *J. acoust. Soc. Am.,* **138**(6), 3864–3872.

Sens-Schönfelder, C. & Eulenfeld, T., 2019. Probing the in situ elastic nonlinearity of rocks with Earth tides and seismic noise, *Phys. Rev. Lett.,* **122,** 138501.

Silver, P.G., Daley, T.M., Niu, F. & Majer, E.L., 2007. Active source monitoring of cross-well seismic traveltime for stress-induced changes, *Bull. seism. Soc. Am.,* **97**(1B), 281–293.

Snieder, R., Sheiman, J. & Calvert, R., 2006. Equivalence of the virtual-source method and wave-field deconvolution in seismic interferometry, *Phys. Rev. E,* **73**(6), 066620.

Snieder, R., Miyazawa, M., Slob, E., Vasconcelos, I. & Wapenaar, K., 2009. A comparison of strategies for seismic interferometry, *Surv. Geophys.,* **30**(4–5), 503–523.

van Eck, T., Goutbeek, F., Haak, H. & Dost, B., 2006. Seismic hazard due to small-magnitude, shallow-source, induced earthquakes in The Netherlands, *Eng. Geol.,* **87**(1–2), 105–121.

Van Thienen-Visser, K. & Breunese, J., 2015. Induced seismicity of the Groningen gas field: history and recent developments, *Leading Edge,* **34**(6), 664–671.

Wegler, U. & Sens-Schönfelder, C., 2007. Fault zone monitoring with passive image interferometry, *J. geophys. Int.,* **168**(3), 1029–1033.

Yamada, M., Mori, J. & Ohmi, S., 2010. Temporal changes of subsurface velocities during strong shaking as seen from seismic interferometry, *J. geophys. Res.,* **115**(B3), doi:10.1029/2009JB006567.

Zhang, H.L., Wang, B.L., Ning, J.Y. & Li, Y.M., 2019. Interferometry imaging using high-speed-train induced seismic waves, *Chinese J. Geophys. (in Chinese),* **62**(6), 2321–2327.

Zhou, W., 2020, Investigating the Groningen gas reservoir: From passive seismic monitoring to experiments on effects of pore pressure on fault slip, *PhD thesis,* Utrecht University.

Zhou, W. & Paulssen, H., 2017. P and S velocity structure in the Groningen gas reservoir from noise interferometry, *Geophys. Res. Lett.,* **44**(23), 11 785–11 791.

Zhou, W. & Paulssen, H., 2019. Travel time changes in the Groningen gas reservoir by train noise interferometry of borehole data, in *Extended Abstracts of 81th EAGE Conference and Exhibition 2019,* pp. 1–5, European Association of Geoscientists & Engineers.

SUPPORTING INFORMATION

Supplementary data are available at *GJI* online.

Figure S1. Train signals recorded on 3 July 2015 at 12:41 (a, c) and 12:46 (b, d). These train signals are half an hour later compared to the ones shown in Fig. 3 of the main text.

Figure S2. Train signals recorded on 27 November 2015 at 17:10 (a, c) and 17:16 (b, d). These train signal are more than 4 months later compared to the ones shown in Fig. 3 of the main text.

Please note: Oxford University Press is not responsible for the content or functionality of any supporting materials supplied by the authors. Any queries (other than missing material) should be directed to the corresponding author for the paper.